THE JOURNAL OF PHYSICAL CHEMISTRY C
A JOURNAL OF THE AMERICAN CHEMICAL SOCIETY

pubs.acs.org/JPCC

Article

# Effective Mass for Holes in Paramagnetic, Plasmonic $Cu_5FeS_4$ Semiconductor Nanocrystals

Jason E. Kuszynski, Joshua C. Kays, Carl R. Conti, III, Stephen A. McGill, Allison M. Dennis, and Geoffrey F. Strouse*

Cite This: *J. Phys. Chem. C* 2022, 126, 12669–12679

Read Online

ACCESS | Metrics & More | Article Recommendations | Supporting Information

**ABSTRACT:** The impact of a magneto-structural phase transition on the carrier effective mass in $Cu_5FeS_4$ plasmonic semiconductor nanocrystals was examined using magnetic circular dichroism (MCD). Through MCD, the sample was confirmed as p-type with variable-temperature studies from 1.8−75 K. Magnetic field-dependent behavior is observed, showing an asymptotic behavior at high field with an $m^*$ value 5.98 $m^*/m_e$ at 10 T and 2.73 $m^*/m_e$ at 2 T. Experimentally obtained results are holistically compared to SQUID magnetization data and DFT calculations, highlighting a dependency on vacancy-driven polaronic coupling, magnetocrystalline anisotropy, and plasmon coupling of the magnetic field, all contributing to an overall decrease in the hole mean free path dependent on the magnetic field applied to $Cu_5FeS_4$.

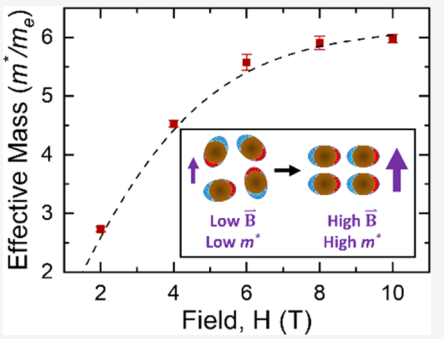




## INTRODUCTION

At the nanoscale, plasmonic materials exhibit a strong localized surface plasmon resonance (LSPR) associated with the oscillation of the Fermi level carriers which induces a large electric field at the nanomaterial surface. Noble metals are the prototypical standard for research on LSPR[1−4] but are typically limited to the visible region.[5] Plasmonic semiconducting nanocrystals (PSNCs) exhibit a plasmon feature that can be systematically tuned from visible to mid-IR frequencies by controlling the carrier density.[6] The tunability of the PSNC LSPR is advantageous for surface-enhanced Raman scattering,[7] refractometric sensing,[8] and photocatalysis.[9] In PSNCs, the frequency of the LSPR is highly sensitive to the number of free carriers and the effective mass of the carriers, as modeled using the simplified Drude model, wherein the plasma resonance frequency ($\omega_p$) (eq 1)

$$\omega_p = \sqrt{\frac{ne^2}{m^*\varepsilon_0}} \tag{1}$$

is assumed to be primarily dependent on both the free carrier density ($n$) and carrier effective mass ($m^*$), where $e$ is the elementary electron charge and $\varepsilon_0$ is the vacuum permittivity constant.[10] The carrier mass is dependent on orbital coupling, will be affected by interband levels, and is impacted by vacancies, surface scattering, and lattice defects. While the high surface area in nanocrystals can influence the measured $m^*$, for simplicity, the carrier mass is typically assumed to be invariant, allowing the plasmon frequency to be predictive of carrier densities. This assumption is reasonable if the only variable is carrier density at a fixed composition and size. The relative difficulty of measuring $m^*$ independently for PSNCs is likely what has led to using the assumption of a constant $m^*$.[11]

In a recent study, it was demonstrated using carrier titration methods that the Drude model underpredicts carrier levels, most likely due to the assumption that the carrier mass is unchanged by the nanoenvironment.[12] Incorporating a p- or n-type dopant into a semiconductor leads to changes in the Fermi level, often accompanied by perturbation of the electron−electron and electron−phonon interactions for a simple valence band (VB)-conduction band (CB) energy structure.[13,14] In such systems, the Drude model will produce a linear trend in LSPR frequency with carrier density as long as vacancies or site occupation changes do not perturb the system. Results from $Sn:In_2O_3$ and M:ZnO (M = Al, Ga, In) show the flaw in ignoring the environment at high carrier concentrations, as site occupation effects lead to charge compensation and deviation from parabolic band theory.[15,16] In these studies, the role of a dampening term ($\Gamma$), as described within the Jung and Peterson model, was proposed to account for the deviation and assumed to be dependent on energy-level parabolicity, in analogy to the recently explored InN system.[17] A change in parabolicity will lead to a change in carrier effective mass. A perturbation of carrier mass at small PSNCs size is not surprising, as the carrier mass will be

**Received:** May 18, 2022
**Revised:** July 13, 2022
**Published:** July 26, 2022

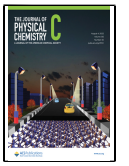




https://doi.org/10.1021/acs.jpcc.2c03459
*J. Phys. Chem. C* 2022, 126, 12669−12679

strongly influenced by scattering, vacancies, and changes in band structure due to surface termination of the nanocrystal.[11,18−21] Clearly, independently measuring $m^*$ and $n$ from experimental data is critical to evaluate the plasmonic field effects in PSNCs accurately.

While many of the PSNCs studied to date are binary or doped binary wide band gap materials,[6] a recent report on the ternary, p-type $Cu_xFeS_4$, otherwise referred to as bornite, has revealed deviation from the simple Drude approximation.[22] $Cu_xFeS_4$ is an intermediate band semiconductor (IBSC), where Fe d-levels occupy the intermediate band states. IBSC systems are increasingly being explored for their thermoelectric properties. They are typically viewed as indirect band gap materials and are expected to be useful for conversion between heat and electricity, photovoltaics, and LEDs.[23−25] The bornite family of PSNCs is of interest for plasmonic systems due to bornite PSNCs' low elemental cost, low toxicity,[26,27] and a biologically transmissive plasmon frequency that is preliminarily an ideal candidate for *in vivo* biomedical applications.[28]

Early studies on nanocrystal bornites have shown the LSPR is invariant with Cu-to-Fe ratio. It was initially hypothesized that changes in the Cu-to-Fe ratio would tune the band filling and thus the LSPR frequency, but experimentally this is not observed. However, a significant LSPR frequency shift is observed by chemical titration, indicating the extinction features to be carrier density-dependent, as expected by the Drude model.[22] The experimental data suggests compensatory effects. These effects differ depending on the Cu-to-Fe ratio and are predicted through a frequency-independent fitting of the Drude model. This results in quantitative damping terms and different effective masses calculated based on the Cu-to-Fe ratio. $Cu_5FeS_4$ (5:1) bornite nanocrystals exhibit a magneto-structural phase transition with a complex spin reorientation, leading to antiferromagnetic (AFM) interactions.[29] The onset of the transition results in an anisotropic structure that impacts the plasmon properties of this PSNC.

The presence of carriers at an LSPR frequency matching the d-band levels influences the carrier effective mass by changing the electron−electron coupling between the LSPR and d-levels. To date, only limited studies on IBSCs have been reported, such as computational studies on $Cu_3MCh_4$ (M = V, Nb, Ta; Ch = S, Se, Te)[30,31] and experimental work on $CuFeS_2$[32,33] and $Cu_3VS_4$.[34] More extensive studies exist for LSPR behavior on Cu chalcogenide direct band gap systems such as $Cu_{1.96}S$ and $Cu_{2-x}Se$.[35,36] The perturbation of the carrier mass in nanocrystals has been reported in p-type binary chalcogenides. In $Cu_{2-x}Se$, the effective mass is observed to be 0.39 $m^*/m_e$ in bulk. However, 0.89 $m^*/m_e$ is determined for nanodisks,[35] while $Cu_{1.96}S$ is observed to have an effective mass of 0.8 $m^*/m_e$, also for nanodisks.[36] Why the carrier mass is perturbed in a nanocrystal has not been fully investigated, and neither has the impact of interband levels on carrier behavior experimentally. This highlights a large gap in the understanding of ISBCs that remains to be filled. This work aims to contribute to filling the gap, as the carrier mass directly impacts carrier mobility for electronic applications and the dampening rate of the plasmon, which affects optoelectronic applications.

In this study, the value of $m^*$ is evaluated for 5 ± 1.4 nm spherical, oleic acid-passivated $Cu_5FeS_4$ PSNCs, the stoichiometric bornite. Variable-field (±10 T) magnetic circular dichroism (VH-MCD) experiments were performed at 40 K to evaluate $m^*$ in the bornite nanocrystal, supplemented with variable-temperature (VT-MCD) experiments from 1.8−75 K measured at 10 T on dropcast thin films of the $Cu_5FeS_4$. Fitting of the VH-MCD spectra revealed a larger than expected $m^*$ for $Cu_5FeS_4$ of 2.73 $m^*/m_e$ at 2 T. An unexpected change in $m^*$ was observed with increasing field, with a nearly asymptotic value of 5.98 $m^*/m_e$ found at 10 T. The observed value of $m^*$ can be understood by the combined contribution of interband polaronic type coupling to the Fe d-bands, magnetocrystalline anisotropy, and light coupled magnetic anisotropy enhancement caused by direct excitation of the LSPR. The effects reduced the overall mean free path of the hole carriers, thereby resulting in the increased $m^*$ value observed for $Cu_5FeS_4$. Additionally, magnetocrystalline anisotropy is expected to perturb the electronic and magnetic properties due to a low-temperature $Cu_5FeS_4$ crystal structure.

## MATERIALS AND METHODS

Copper (II) acetylacetonate ($Cu(acac)_2$, 97%), iron (III) acetylacetonate ($Fe(acac)_3$, ≥99.9%), 1-dodecanethiol (DDT, ≥98%), oleic acid (OA, technical grade, 90%), oleylamine (OLA, technical grade, 70%), and poly (lauryl) methacrylate in toluene (PLMA, 25%) were purchased from Sigma-Aldrich. Tetrachloroethylene (TCE, 99.0%) was purchased from Beantown Chemical. Quartz glass substrates were sourced from GM-Quartz, while VGE-7031 varnish was sourced from Lake Shore Cryotronics, Inc. Size #4 gelatin capsules for SQUID measurements were obtained from Electron Microscopy Sciences.

**Synthesis of $Cu_5FeS_4$ Nanocrystals.** $Cu_5FeS_4$ PSNCs were prepared following previously reported methods.[22] Briefly, $Cu(acac)_2$ (261.8 mg, 1.0 mmol) and $Fe(acac)_3$ (70.63 mg, 0.2 mmol) (Cu/Fe ratio of 5:1) were dissolved in 6.7 mL of oleic acid in a three-neck flask under Ar. After heating the solution to 180 °C, 1.5 mL of dodecanethiol was rapidly injected, followed by a 5 min drop-by-drop addition of a solution of sulfur dissolved in oleylamine (0.2 M, 15 mL). The reaction was maintained at 180 °C for 5 min and cooled to room temperature. The $Cu_5FeS_4$ was transferred to a glovebox after it had reached room temperature and stored under an Ar atmosphere. ICP-MS analysis verified the 5:1 ratio of Cu to Fe. TEM analysis confirms the formation of spherical 5 ± 1.4 nm nanoparticles, and p-XRD analysis matches the high cubic bornite phase commonly seen at higher temperatures.[37] (Figure S1)

**Linear Absorption Spectroscopy.** $Cu_5FeS_4$ PSNCs were suspended in TCE and diluted until an LSPR absorption of approximately 1.0 absorbance was obtained. UV−vis−NIR measurements were collected in a 1 cm NIR optical cell (Spectrocell) on a PerkinElmer Lambda 950 spectrophotometer. Spectra were baseline-corrected using neat TCE and normalized to the band-edge absorption of the PSNCs. Additionally, samples were dropcast onto quartz substrates, verified by the Lambda 950 spectrophotometer at room temperature before cryostat insertion, and scanned via linear absorbance at 40 K within the cryostat.

**MCD Sample Preparation.** Thin films of $Cu_5FeS_4$ nanocrystals were prepared by dropcasting the colloidal TCE solution onto a quartz substrate. Poly(lauryl) methacrylate (PLMA) was added as a binder to assist with adhesion to the substrate. Concentration was controlled and monitored by checking the sample substrate using a Lambda 950 UV−vis−NIR spectrometer until an optimal absorbance of approximately 1.0 is obtained. Afterward, VGE-7031 varnish was used


https://doi.org/10.1021/acs.jpcc.2c03459
J. Phys. Chem. C 2022, 126, 12669−12679

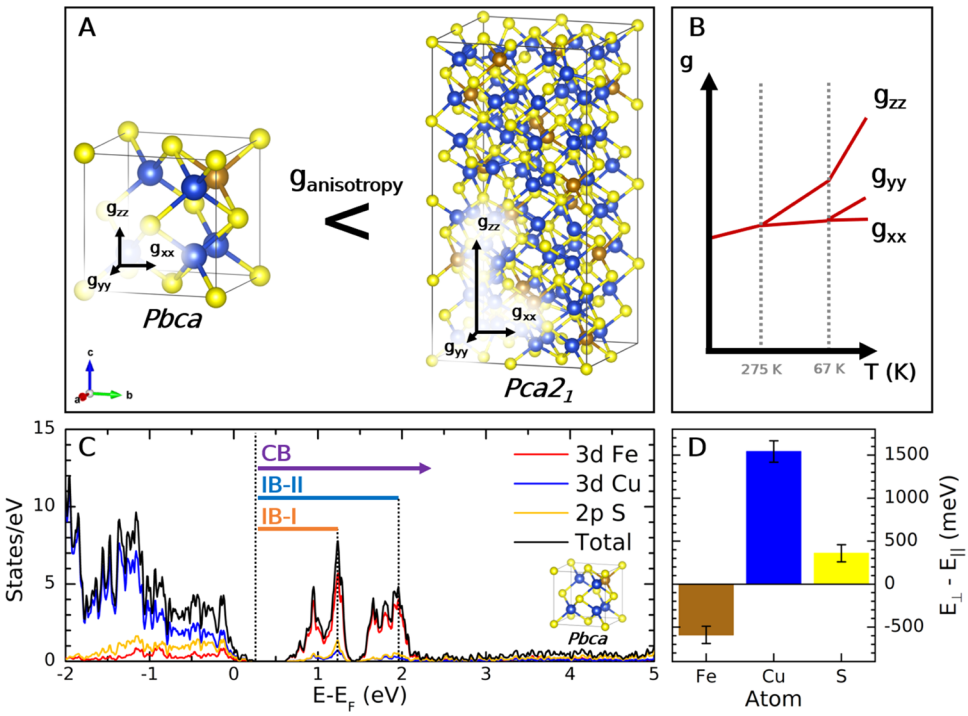


**Figure 1.** Theoretical Investigation of $Cu_5FeS_4$. (A) Cubic $Cu_5FeS_4$ unit cell used in calculations for this work is compared to the low-temperature $Pca2_1$ phase[41] with expected *g*-factor vector differences. Sulfur atoms are yellow, copper blue, and iron brown. (B) Expected *g*-factor splitting behavior as a function of temperature with a breaking of symmetry initially occurring at 275 K for *Pbca and then occurring again at 67 K for* $Pca2_1$. *(C) Representative DOS plot identifying high probability electronic transitions and showing the expected IBSC structure. (D) DFT calculations were used to calculate magnetic anisotropy energy (MAE) for perpendicular versus parallel magnetic moment orientations for the unit cell and broken down by atomic differences.*

to adhere the substrate onto an optical probe for use in the cryostat.

**Variable-Field (±10 T at 40 K) Magnetic Circular Dichroism (VH-MCD).** The variable-field VH-MCD is performed on the $Cu_5FeS_4$ sample dropcast onto a 0.5 in quartz substrate. The sample was dried under vacuum prior to insertion into an Oxford Instruments 10 T HelioxTL Superconducting Spectromag. A Newport Quartz Tungsten Halogen Lamp (Model 70050) with a monochromator (Model 69931) and optical chopper operating at a frequency of 211 Hz was used in combination with a ThorLabs Glan−Taylor linear polarizer (GLB-10) to linearly polarize incident light, followed by use of a HINDS Instruments photoelastic modulator (PEM-100) for subsequent circular polarization at 47 kHz. Two Stanford Research Systems SR830 lock-in amplifiers were phase-locked to the chopper and PEM frequencies to maximize the signal-to-noise for the DC detector spectrum ($V_{DC}$) and $\Delta A$ signal ($V_{AC}$) obtained, respectively. A Thorlabs biased Si photodetector (DET10A) and a biased InGaAs detector (DET20C2) were used interchangeably to select for visible and NIR regimes, respectively, and amplified with a Femto current amplifier (LCA-200K-20M). Temperature was monitored and controlled through a Keck clamp fiber cable routed through the sample probe and mounted adjacent to the sample substrate. A positive and negative field sweep scan from 0−10 T was performed for the bornite samples at 40 ± 1 K in 2 T intervals. The reported spectra were corrected by subtracting the 0 T scan to eliminate artifacts from polarization effects, magnetic field inhomogeneity, and other disturbances that may arise during MCD measurement. To confirm polarization of the experimental setup, a 6.2 nm gold nanoparticle solution was compared to a cast film of Au NP measured in the sample cavity of the cryostat versus the fringe field (for reference, the field reduction at the outer window is 10 to 6T and follows an exponential decay with distance) of the cryostat. The experimental calibration results agree with published data[35] and confirm the experimental setup is properly corrected. (Figure S2). Positive and negative field magnetic vector directions were confirmed through the use of a right circularly polarized film to identify whether to subtract positive field data from negative or negative from positive when performing the difference measurements in the Faraday configuration.

**Variable-Temperature (1.8−75 K at 10 T) Magnetic Circular Dichroism (VT-MCD).** The same experimental setup used for VT-MCD measurements was used: while holding the applied magnetic field at +10 T, the temperature was swept from a minimum temperature of 1.8 to 75 K, where three scans were taken at each temperature point and averaged utilizing the InGaAs NIR detector to measure C-term contributions at and near the LSPR feature.

**VH-MCD Effective Mass Fitting.** From the spectra, experimental absorption spectra are used as the basis for a rigid-shift simulation of LCP and RCP absorption as a function of $E_z$ to fit the experimental VH-MCD spectra. The simulated MCD fit is optimized by a custom Python code at each field, allowing for the direct measurement of $E_z$ and $m^*$ at every measured magnetic field, thereby increasing the accuracy and robustness of MCD measurements. The acquisition of $m^*$ through MCD itself is not novel; however, the acquisition through comparison by RS approximation of a corresponding absorption spectrum is nontrivial.[35] The novelty originates from the spectral range and standardization of data analysis,


https://doi.org/10.1021/acs.jpcc.2c03459
J. Phys. Chem. C 2022, 126, 12669−12679

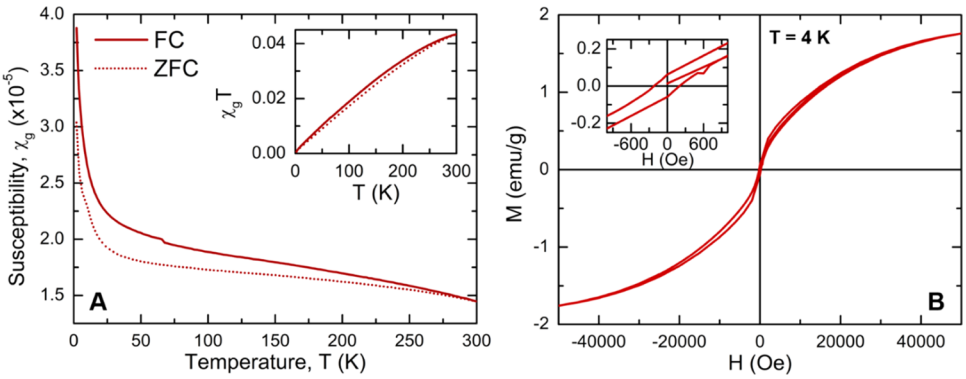


**Figure 2.** Magnetic Data of $Cu_5FeS_4$ PSNCs. (A) Magnetic susceptibility measurements show a high degree of coercivity between FC and ZFC curves, with the previously reported antiferromagnetic transition at 67 K[41] observed as a discontinuity. Additionally, the majority of linear behavior seen in $\chi$T (A, inset) indicates the presence of long-range antiferromagnetic ordering. (B) Magnetization measurements were performed at 4 K, showing a narrow hysteresis loop that indicates weak coercivity approaching the single domain, superparamagnetic regime for the $Cu_5FeS_4$ PSNCs.

which allows for multiple collections of $m^*$ from only one experimental MCD run, which sweeps through various magnetic field strengths, and every field integer can subsequently be treated as its own experiment. Simulated MCD spectra are calculated using the Scipy.optimize.curve_fit-() Python function utilizing the trust region reflective algorithm to provide a simulation of best fit using $E_z$ as the dependent variable for minimization. The python code used is publicly available at https://github.com/strouselabgithub/strouselab.

**Superconducting Quantum Design MPMS SQUID Magnetometry.** Field and Temperature sweep SQUID magnetometry was performed on $Cu_5FeS_4$ diluted in eicosane (1:10 mg) and loaded as a powder in gel capsules. The dilution in eicosane is to minimize particle−particle interactions. Magnetization data was collected at 4 K from −50 to 50 kOe, while magnetic susceptibility data was recorded at 1 kOe for field sweep and no field for the zero-field sweep measurements from 2−300 K.

**Computational Details.** DFT + U calculations were performed to simulate the projected density of states for $Cu_5FeS_4$ utilizing the open-source Quantum ESPRESSO repository.[38] A single unit cell of $Cu_5FeS_4$ was initialized with lattice constants of 5.475 Å, similar to prior literature.[37] Plane augmented wave pseudopotentials were used in addition to unrestricted DFT + U, as was used previously for $CuFeS_2$.[32] Self-consistent field calculations were performed on a relaxed structure with a Monkhorst k-point mesh of 6 × 6 × 6 to maximize sampling across the dielectric field of the Brillouin zone.[39] This was followed by a non-self-consistent field calculation of 12 × 12 × 12 for the simulated projected density of states. Simulated absorption spectra and transitions of interest were acquired by diagonalizing and solving for allowed transitions after calculating the density of states (DOS). Magnetic anisotropy energy (MAE) was calculated using the Force Theorem method[40] by comparing the total energy of the system under perpendicular and parallel magnetic orientations.

## RESULTS AND DISCUSSION

Bulk 5:1 bornite exhibits a second-order magnetic—structural phase transition at 67 K that is coupled with a structural phase transition from *Pbca* to $Pca2_1$ resulting in a loss of higher-order symmetry at $T < 67$ K.[41,42] The second-order transition in the bulk sample is described as a RT paramagnetic-to-low-temperature antiferromagnetic (PM-AFM) transition but can be thought of as a spin glass transition due to spin reordering. The structural shift from *Pbca* to $Pca2_1$ will induce changes in *g*-factor tensors, as shown in Figure 1A. The presence of the structural-magnetic phase transition leads to a complex spin-ordering event, causing increased magnetocrystalline anisotropy reminiscent of a Bose−Einstein condensate.[43] The increased anisotropy will impact carrier mass, as seen in the anisotropic crystal structure of anatase $TiO_2$.[44] In the case of 5:1 bornite, this will be dependent on the strength of the applied magnetic field, leading to anomalous Zeeman splitting for the electronic transitions. This can be explained as resulting from the nonlinear *g*-factor changes occurring as a function of decreasing temperature and modeled after the changes in unit cell parameters observed by Rietveld refinement.[41]

**Computational Predictions.** In Figure 1, the impact on the electronic levels of the *Pbca* to $Pca2_1$ structural change for 5:1 bornite (Figure 1A) can be evaluated by considering the anticipated splitting of the electronic levels in a magnetic field (Figure 1B). The change in energy with the field can be rewritten in terms of the anisotropic *g*-values (eq 2)

$$g = (g_{xx}^2 \sin^2\theta \cos^2\phi + g_{yy}^2 \sin^2\theta \sin^2\phi + g_{zz}^2 \cos^2\theta)^{1/2} \quad (2)$$

In the case of the $Pca2_1$ structure, when only considering lattice parameters, $g_{xx} \neq g_{yy} \neq g_{zz}$. Schematically, this is represented in Figure 1B and illustrates the importance of considering the evolution of *g*-factor contributions under a magnetic field as a function of temperature. In the case of 5:1 bornite, as temperature decreases, the disparity in anisotropic *g*-values increases and directly correlates to a rise in magnetocrystalline anisotropy that should be observable experimentally.

Figure 1C,D presents the predicted electronic structure and magnetocrystalline anisotropy as the calculated projected density of states (DOS) and magnetic anisotropy energy (MAE). The MAE and DFT calculations were performed on a reduced unit cell (Figure 1A) using Quantum ESPRESSO density functional theory (DFT) self-consistent field calculations.[38] Consistent with literature precedent,[45] the 5:1 bornite has a band gap of approximately 2.09 eV with two intermediate band gaps of 0.22 and 1.12 eV associated with Fe tetrahedral d-level splitting. The Fermi level beneath the valence band edge (Figure 1C) also agrees with the assignment


https://doi.org/10.1021/acs.jpcc.2c03459
J. Phys. Chem. C 2022, 126, 12669−12679

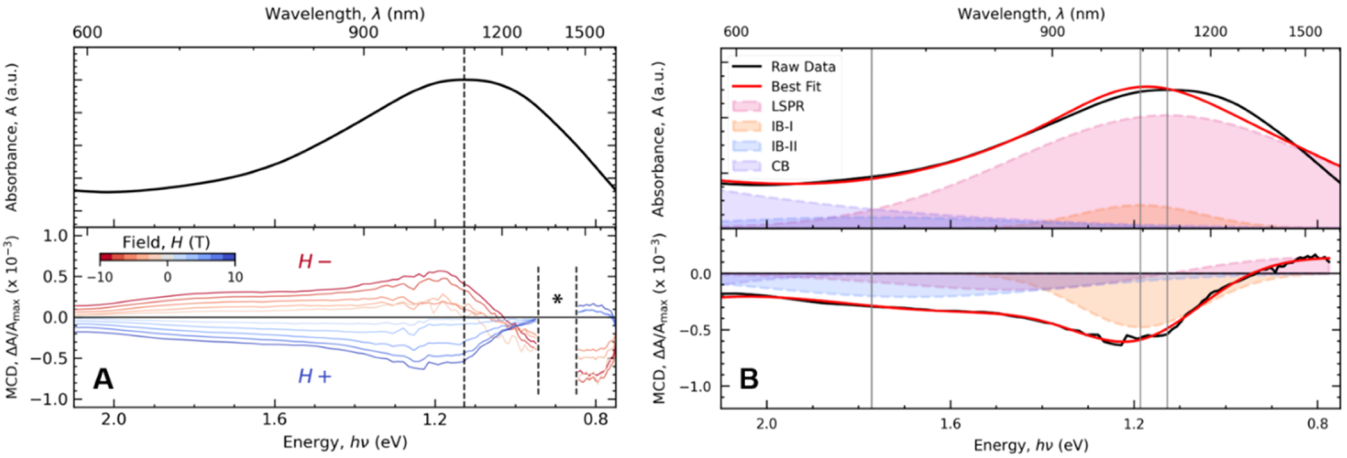


**Figure 3.** Magneto-optical data of $Cu_5FeS_4$ PSNCs. (A, top) Characteristic 40 K linear absorption spectrum of 5 nm $Cu_5FeS_4$ is shown with an LSPR extinction feature observed at 1.1 eV and indirect band gap at 2.1 eV paired with (A, bottom) VH-MCD data taken for $Cu_5FeS_4$, where the VH-MCD data is merged from a visible Si detector and a near-infrared InGaAs detector. The LSPR peak observed in linear absorption is slightly higher in energy compared to the inflection point observed in the VH-MCD spectra (1.1 vs 1.0 eV as denoted by the dashed line). A discontinuity in data for the VH-MCD data is removed at 0.9 eV marked by the asterisk attributed to a characteristic transmission dip observable in Spectrosil B windows. The full, unmodified spectra can be found in Figure S3. (B, bottom) MCD Data at 10 T is deconvoluted by several probable electronic transitions observed in the previously performed DOS calculations. (B, top) Subsequently, the linear absorption is reconstructed utilizing the same transition energies and FWHM, letting the amplitude float as the spectra is fitted with the Scipy.optimize.curve_fit() least-squares fitting algorithm. Gray vertical lines mark the various transitions assigned.

of a p-type IBSC system. Hybridization between Cu-3d and S-2p is evident in the valence band in the DOS.

To calculate the MAE, Quantum ESPRESSO uses ultrasoft pseudopotentials in the generalized-gradient approximation selected through the standard solid-state pseudopotential library[46−48] to generate a semi-quantitative understanding of MAE utilizing the Force Theorem method.[40] This allows the total electronic band energy to be differentiated between perpendicular and parallel magnetic dipole moments. The value of the full MAE is 2.14 eV on average between the Fe(III) atom and the averaged Cu(I) atoms. Cu shows the greatest deviation in magnetic dipole moment, favoring a parallel magnetic dipole, while Fe favors a perpendicular magnetic dipole orientation. While S should possess no magnetic moment, it is hypothesized that an MAE is experienced for these atoms due to orbital hybridization of the Cu-3d with S-2p, as observed in the DOS. The observed hybridization is expected to introduce magnetic coupling between these two electronic states in the form of p−d orbital exchange coupling.[49] As the observed extinction feature in an LSPR mode is reflective of the imaginary and real component crossing of the dielectric function, it is anticipated the LSPR mode will be impacted by the magnetic anisotropy, especially considering the carriers originate from Fe vacancies.[45]

**Magnetic Properties.** In Figure 2A, the onset of antiferromagnetic (AFM) order is observed as a discontinuity at 67 K in temperature-dependent magnetic susceptibility (2−300 K) measurements using a superconducting quantum interference device (SQUID). The inset of Figure 2A shows a strong linear trend up to 300 K for the $\chi$T data, indicating typical paramagnetic behavior associated with the DOS projected Fe-3d intermediate band level.[22,45] The field sweep data and zero-field-cooled (ZFC) vs field-cooled (FC) temperature sweep data reveal the 5:1 bornite is magnetic with increased coercivity as temperature decreases for $Cu_5FeS_4$. The assignment of an AFM magnetic transition at the magnetic susceptibility discontinuity agrees with prior bulk bornite experiments, where collinear AFM ordering of spins, parallel and antiparallel to the *b*-axis, was reported at $T_N$ = 67.5 K. Ferrimagnetic order appearing below 35 K was associated with charge ordering.[42,50−52] In the bulk bornite, a fluctuation of the spins below 140 K associated with Fe and Cu is observed to produce a magnetic moment with spin orientation that changes due to valence fluctuations. The second-order phase transition at 67.5 K couples the magnetic and lattice (*Pbca* to $Pca2_1$) elements, resulting in a structural dependence of electron exchange via the induced crystalline anisotropy following the transition. The structural transition results in a superparamagnetic relaxation, leading to a loss of higher-order symmetry, increasing magnetocrystalline anisotropy in the 5:1 bornite.[53] The magnetic and structural properties are associated with temperature-dependent intervalence charge fluctuation ($Fe^{3+/2+}$, $Cu^{2+/1+}$) in the 5:1 stoichiometry below 140 K.

Consistent with the MAE and magnetic measurements, the 5:1 bornite PSNC is anticipated to have a large magneto-crystalline anisotropy caused by the loss of crystallographic symmetry. As the bornite PSNCs themselves are spherical, shape anisotropy is precluded from contributing significantly and is not considered here. The coercivity at 4 K is 200 Oe and saturated magnetization, $M_{sat}$, is 1.8 emu/g. However, this is likely due to nearing the superparamagnetic regime for these nanocrystals, as they are well within the typical size regime of <10 nm.[54] Utilizing eqs 3 and 4, the effective magnetic anisotropy, $K_{eff}$, and superparamagnetic diameter threshold, *D*, can be estimated utilizing the observed blocking temperature, $T_b$, of 299 K and calculating for the volume, *V*, of a typical 5 nm nanocrystal

$$T_b = \frac{K_{eff}V}{25k_B} \tag{3}$$

$$D = \sqrt[3]{\frac{31k_BT}{K_{eff}}} \tag{4}$$



https://doi.org/10.1021/acs.jpcc.2c03459
J. Phys. Chem. C 2022, 126, 12669−12679

where $k_B$ is the Boltzmann constant and $T$ is the temperature. For $Cu_5FeS_4$, a $K_{eff}$ of 0.197 MJ/m$^3$ and $D$ of 1.58 nm at 4 K are predicted for $Cu_5FeS_4$, agreeing with the experimental data observed.

**Optical Properties.** As shown in Figure 3, the p-type $Cu_5FeS_4$ PSNC exhibits a well-defined LSPR at 1.1 eV. Our previous publication evaluated the LSPR using the Drude model approximation. We concluded that the carriers arose from Fe vacancies with a Drude model-predicted effective mass of 1.4 $m^*/m_e$ at RT.[22] As the temperature decreases, carrier mass is expected to increase with the lattice valence ordering. Assuming the onset of AFM order is the same as the reported bulk bornite, charge fluctuation is anticipated to strongly influence the effective carrier mass and thus plasmon properties below 140 K, leading to nonlinear Zeeman effects.[51,55] The effect of the magnetic field on the carrier mass can be evaluated using MCD below the magnetic phase transition to calculate the effective carrier mass ($m^*$) from the cyclotron resonance frequency,[35] as MCD exploits two magneto-optical phenomena in tandem, cyclotron resonance and the Zeeman effect, both of which are described in previous literature with respect to MCD.[56−58] Evaluating the field-dependent change in $m^*$ above and below the AFM ordering temperature in the 5:1 bornite PSNC should allow carrier density changes expected to occur with valence ordering in the anisotropic low-temperature 5:1 crystal lattice to be simulated using the Drude model.

MCD is useful for its sensitivity to site-specific metal contributions in a given material.[59] MCD has been previously used to elucidate fine structures that may appear in optical features such as band gap absorption edges in semiconductors, intra-atomic transitions, and LSPRs.[60−62] The MCD spectra are plotted as the difference spectra ($\Delta A$) of left circularly polarized light (LCP) absorption subtracted from right circularly polarized light (RCP) absorption, where LCP is selective for $\Delta M_J = +1$ while RCP is selective for $\Delta M_J = -1$. These selection rules allow for energy shifting in the LCP and RCP absorption spectra.[57] The difference in energy for LCP and RCP absorption for spin levels of the electronic system is termed the Zeeman effect. The magnitude of the Zeeman effect is contingent on the degree of splitting proportional to magnetic field strength rather than originating from a property intrinsic to the material itself, such as chirality for circular dichroism. The Zeeman effect is represented by the splitting of the electronic energy level induced by the application of an external magnetic field, represented mathematically as (eq 5)

$$E_Z = g u_B M_J \vec{\mathbf{B}} \tag{5}$$

where $g$ is the $g$-factor, $u_B$ is the Bohr magneton, $M_J$ is the total angular momentum, and $\vec{\mathbf{B}}$ is the total magnetic flux in the material.[57] The Zeeman splitting energy ($E_Z$) is fundamental to magneto-optical spectroscopy and allows for the observation of electronic transitions that would otherwise be impossible for traditional optical techniques. The carrier type (n or p) is evaluated by inspection of the sign of the LCP absorption feature, with p-type showing a positive LCP and n-type exhibiting a negative LCP feature.

By assuming Born−Oppenheimer, Franck−Condon, and rigid-shift (RS) approximations, the $\Delta A$ MCD spectrum can be deconvoluted into three constituent shapes classified as $A_1$, $B_0$, and $C_0$ terms (eq 6)[56]

$$A_1 : B_0 : C_0 = \frac{1}{\Gamma} : \frac{1}{\Delta E} : \frac{1}{k_B T} \tag{6}$$

where $\Gamma$ is the absorption feature linewidth magnitude, $\Delta E$ is the zero-field state separation magnitude, $k_B$ is the Boltzmann constant, and $T$ is the temperature.[56] The $A_1$-term originates from the lifting of degeneracy in the nearest excited state due to Zeeman splitting directly proportional to the magnetic field applied to the sample. $A_1$-term effects are broadly identifiable from their derivative-shaped curve, where both a positive and negative feature will be present in the differential spectrum. $A_1$-terms are extremely useful for determining the precise energy level of an electronic orbital at zero-field by examining where inflection points appear. The $B_0$-term is unique because it arises from the population mixing of neighboring, non-degenerate excited states at zero-field. As a magnetic field is applied, the change in the mixing of populated states accounts for differences observed in a $B_0$-term feature. $C_0$-term effects could be considered an opposite process relative to the $A_1$-term, as nondegeneracy arises in the ground state of an electronic transition under an applied magnetic field. In 5:1 bornite PSNCs, the magneto-structural phase transition will lead to crystalline anisotropy and a magnetic ground state, resulting in $A_1$- and $C_0$-term contributions to the MCD spectra. $C_0$-term contributions are typical in paramagnetic systems.[56]

In Figure 3, linear absorption and variable-field MCD (VH-MCD) from 10 to −10 T are measured on dropcast films of $Cu_5FeS_4$ at 40 K between 600 and 1700 nm, as seen in Figure 3A and B, respectively. The experimental data is collected on substrate-cast films inserted into a He-cryostat and requires separate data collection regions due to limits in spectral sensitivity of the detectors available. The MCD spectra are plotted as the measured difference ($\Delta A/A_{max}$) between LCP and RCP spectra. A transmission dip at 0.9 eV is attributed to a small absorption in Spectrosil B Quartz which, while not visible in the linear absorption, is likely due to the lower signal and sensitivity of the VH-MCD data. In Figure 3A, the MCD inflection is not centered on the LSPR peak. The offset may be due to underlying overlapping transitions with different Zeeman energies or, more likely, inter-particle coupling in the cast film, as observed in gold plasmonic nanomaterials.[63,64]

For the linear absorption compared with previously performed colloidal solution measurements,[22] an overall increase in inter-particle scattering is observed for $Cu_5FeS_4$, coincident with an increase in the FWHM. Across multiple samples prepared using various dropcasting methods, the observed thin-film spectra are consistent and reproducible, pointing to a real change in the dielectric function. Fitting the frequency-independent simplified Drude model utilizing the MATLAB code from Milliron and co-workers[10] was used to quantify these observed differences in terms of the plasma frequency ($\omega_p$) and damping term ($\Gamma$) for $Cu_5FeS_4$, using 3.48 as the dielectric constant of $Cu_5FeS_4$,[55] as shown in Figure S4 in the Supporting Information. The changes in the frequency and damping contributions between temperatures are quantified by subtracting the room temperature fits from the 40 K results, where $Cu_5FeS_4(\Delta\omega_p)$ = 1201.7 cm$^{-1}$, $Cu_5FeS_4(\Delta\Gamma)$ = 5791.14 cm$^{-3}$. These results show that the damping observed in the dropcast $Cu_5FeS_4$ sample is significantly greater compared to the colloidal solution, supportive of an increase in overall inter-particle effects, donor level scattering,[65] or changes in the local dielectric.



https://doi.org/10.1021/acs.jpcc.2c03459
J. Phys. Chem. C 2022, 126, 12669−12679

**Table 1. MCD and Absorption Fitting Parameters**

| peak assignment | energy (eV) | $A_1$ ($C_0$)/D | $B_0$/D ($eV^{-1}$) | Abs FWHM (eV) | Abs amplitude (a.u.) |
|---|---|---|---|---|---|
| LSPR | 1.12 | $-8.29 \times 10^2$ | --- | 0.8 | 0.409 |
| IB-I | 1.19 | $-3.89 \times 10^1$ | $-9.76 \times 10^3$ | 0.32 | 0.086 |
| IB-II | 1.77 | $2.02 \times 10^3$ | $-8.52 \times 10^3$ | 0.76 | 0.041 |
| CB | 3.44 | $3.70 \times 10^4$ | $-9.18 \times 10^{-3}$ | 1.01 | 0.186 |

The VH-MCD spectra in Figure 3A can be evaluated in terms of the $A_1$- (Zeeman term), $B_0$- (field-induced state mixing), and $C_0$- (ground state degeneracy due to paramagnetic state) terms (eq 7).

$$\frac{\Delta D_{MCD}(E)}{E} = \gamma\left\{A_1\left(-\frac{df(E)}{dE}\right) + \left(B_0 + \frac{C_0}{kT}\right)f(E)\right\}(\mu_B H)cz \quad (7)$$

where $\Delta D_{MCD}(E)$ is the MCD spectrum, $E = h\nu$ for photon energy, $\gamma$ is an oscillator strength constant, $f(E)$ is the linear absorption spectra normalized by area, $k_BT$ is the Boltzmann constant and temperature product, $\mu_B$ is the Bohr magneton, $H$ is the field strength, $c$ is the concentration, and $z$ is the pathlength.[58,66] The 5:1 bornite is magnetic and may have $C_0$-term contribution. The coupled structural and magnetic phase transition below 67 K may impact the value of $C_0$. It is anticipated that the ratio of $A_1/B_0/C_0$ is the same as in eq 6 (1:10:200 for this experiment at 40 K).[67] The temperature dependence of the MCD signal for the LSPR band and IB-I was measured at 10 T from 75−1.8 K to evaluate the magnitude of the $C_0$ contribution (Figure S5). As the second-order magneto-structural phase transition occurs at 67 K, it is anticipated that a temperature-dependent MCD response may be observable from 75−1.8 K, reflecting the onset of spin-carrier interactions. The lack of MCD spectral change with temperature in the phase transformation region at 10 T suggests the MCD data is dominated by the $A_1$ ($C_0$) and $B_0$ terms in eq 7 for the 5:1 bornite due to the maximization of magnetic dipole orientation along the high $m^*$ axis at 10 T. At a lower magnetic field, a temperature dependence is expected, as the magnetic dipole is not maximized in one vector orientation; however, further studies are needed to validate this hypothesis.

In Figure 3, the experimental data are fitted to a convolved $A_1$: $C_0$ and $B_0$ term. The deconvolution of peaks is formed by the summation of a Gaussian curve representing $C_0$ and $B_0$ terms and the derivative of a Gaussian curve representing the $A_1$ term modeled after previous literature.[66] The assigned electronic transitions in the MCD at 1.12 (LSPR), 1.19 (IB-I), 1.77 (IB-II), and 3.44 (CB) eV are identified through second-order derivation of the linear absorption spectrum in tandem with the most probable computationally identified electronic transitions. For the fits, the normalized transition dipole moments were obtained as indicated previously by Safin et al.[66] The assumption of a $B_0$ contribution and a convolved $A_1$-: $C_0$-term reflect the known magnetic ground state in 5:1 bornite and the difficulty to deconvolve the MCD spectra fully. MCD parameters for the identified transitions are listed in Table 1.

The LSPR and IB-I (VB → d-band (Fe-$e_g$)) transitions are dominated by the convoluted $A_1/C_0$ term contributions (referred to as $A_1$ term henceforth), while IB-II (VB → d-band (Fe-$t_{2g}$)) and CB transitions have $A_1$ and $B_0$-term contributions, indicating that there is a high degree of mixing of energy levels present in these band regions. The $B_0$ contribution in IB-II reflects the low $\Delta E$ of the split $t_2g$ level compared to IB-I (Figure 1). The CB exhibits the largest $A_1$-term, reflecting the multitude of excited state transitions that can occur within the CB. The MCD fits show negative $A_1$ term dichroism for the LSPR and IB-I transitions, while the IB-II and CB show positive dichroism. The negative $A_1$-term for the LSPR transition experimentally confirms that the 5:1 sample is a p-type PSNC.[35,68] The observed opposite dichroism correlates to antiparallel magnetic moments for the Cu 3d and Fe-3d orbitals below the AFM ordering temperature in 5:1 bornite. Fe vacancies are theorized to be the source of free holes in chalcopyrite, $CuFeS_2$, and are suspected of having the same origin for the carriers generating the p-type LSPR for bornite-like semiconductors.[43,69] The observation of the same dichroism for LSPR and IB-I likely indicates that the carriers are in the IB-I Fe-3d ($e_g$) bands.

*Effective Mass Calculation.* From the MCD spectral assignments, $m^*$ can be evaluated using the relationship in eqs 8 and 9

$$m^* = \frac{qB}{\omega_c m_e} \quad (8)$$

$$\omega_c = \frac{2\pi E_Z}{c} \quad (9)$$

where $\omega_c$ is the cyclotron resonance frequency, $q$ is the elementary charge, $B$ is the magnetic field, $m_e$ is the mass of an electron, $E_z$ is the Zeeman splitting, and $c$ is the speed of light. Assuming the LSPR will obey the RS approximation, as previously reported by Gamelin and co-workers,[35] the LCP and RCP spectra will split equally about the LSPR frequency, resulting in the observed MCD spectrum (Figure S6). The field-dependent splitting yields a Zeeman splitting value ($E_z$) as observed in eq 5.[57,70] In Figure 4, the Zeeman term as a function of the applied field is plotted and exhibits an

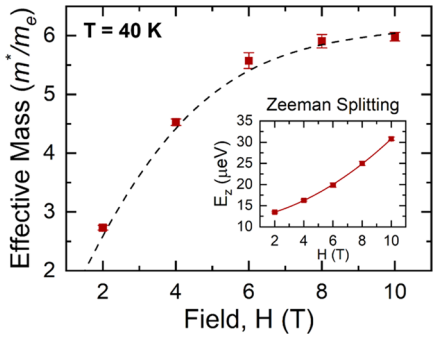


**Figure 4.** Effective Mass Behavior in $Cu_5FeS_4$ PSNCs. VH-MCD for $Cu_5FeS_4$ were fitted with simulated MCD spectra to obtain a Zeeman splitting energy ($E_z$) for all collected fields at 40 K. Once $E_z$ is calculated, $m^*$ is solved for utilizing a convolution of eqs 8 and 9, where a magnetic field-dependent behavior is observed. A sigmoidal-like increase in $m^*$ is observed until 10 T, where $m^*$ approaches an asymptote of 5.98 $m^*/m_e$ and is fitted to a Brillouin function (dotted line), with $S = 1/2$. The raw $E_z$ fit data (inset) is shown to also increase in a nonlinear fashion and is fit to a 5/3 power law.



https://doi.org/10.1021/acs.jpcc.2c03459
J. Phys. Chem. C 2022, 126, 12669−12679

asymptotic behavior. The asymptote reflects the field-driven spin orientation of the spin lattice in the 5:1 bornite, consistent with the model developed for bulk bornites.[42,51]

A plot of the field-dependent $m^*$ for 5:1 bornite is shown in Figure 4. A complete description of the $m^*$ calculation can be found in the Supporting Information. The $m^*$ exhibits a field-dependent effective mass that can be fitted to a hyperbolic cotangent arising from the spin-ordering saturation at high fields, consistent with the SQUID data. The value of $m^*$ exhibits a minimum of 2.73 ± 0.041 $m^*/m_e$ at 2 T and a maximum of 5.98 ± 0.074 $m^*/m_e$ at 10 T. The calculated value for $m^*$ at 2 T is high but not unreasonable for a p-type semiconductor system with intrinsic Fe vacancies present in the crystal structure. As the concentration of vacancies increases, the increase in scattering centers will dampen the carrier mobility and be reflected in the $m^*$ value. Combined with the previously discussed DFT results, as the valence band is primarily composed of S-2p and Cu-3d and IB is composed of Fe-3d, the field-dependent $m^*$ behavior can be correlated and understood through the increased band overlap due to high field Zeeman splitting increasing the degree of the p−d exchange interaction.[49]

When compared to similar Cu-based p-type systems, the $m^*$ values calculated are within reason.[71] For example, Kumar et al. observed an increase in carrier mobility and a subsequent decrease in effective mass through the doping of Se.[72] Although no bulk measurement of pure $Cu_5FeS_4$ could be obtained, the nearest ratio $Cu_5FeS_{3.9}Se_{0.1}$ was measured to have an $m^*$ of 2.56. However, with the degree of carrier mobility shift due to Se doping, it is likely that the intrinsic $m^*$ for $Cu_5FeS_4$ is much higher than what could be effectively measured using the Hall effect. With an observed significant increase in resistivity and decrease in carrier mobility, one would expect the $m^*$ for bulk bornite to be higher than 2.56 $m^*/m_e$, which corresponds with the directly measured 2 T $m^*/m_e$ from VH-MCD in this paper. Utilizing prior data from bulk $Cu_5FeS_4$, a constant carrier relaxation time approximation is used to extrapolate what the undoped $Cu_5FeS_4$ value may be, utilizing a Se doped system previously published, as shown in Figure S7. From a first-order, linear approximation between $m^*$ and the electron mobility, the predicted $m^*$ for a bulk $Cu_5FeS_4$ is near 2.71 $m^*/m_e$ under no applied magnetic field, matching surprisingly well to the MCD experimental data. Yet, it does not explain the asymptotic behavior seen as the effective mass rapidly increases with increasing field.

As reported by Pineider, a possibility for the increased $m^*$ value is neighboring electronic interband transitions leading to variation in the local dielectric function.[73] From the DFT calculations and literature, interband coupling may impact the local dielectric function.[22] However, the interband mixing alone would not account for the observed enhancement of $m^*$. Previous work with $Cu_{2-x}Se$, featuring very similar optical absorption and MCD $A_1$-term asymmetry, also reported differences in bulk versus nanocrystal $m^*$ due to changes in carrier compensation.[35] The observation of a large $m^*$ in anatase $TiO_2$ is thought to arise from crystalline anisotropy, resulting in differences in carrier mobility along separate axes of the crystal structure.[44] In Au/Co/Au film nanostructures, excitation of the LSPR under an applied magnetic field resulted in a strengthening of magnetic anisotropy along a given crystallographic axis.[74] Similarly, the magnetocrystalline anisotropy is anticipated to impact the MCD spectra for 5:1 bornite due to the previously reported magneto-structural transition at 67 K[41] and photoexcitation from the MCD experiment itself.

The presence of the hyperbolic field-dependent $m^*$ values suggests that a major contributor to the large $m^*$ value is the coupling of the spins on the iron and Cu center to the holes in 5:1 bornite. The stronger coupling at a high magnetic field will lead to a greater degree of phonon−hole coupling to the lattice from the observed magnetocrystalline anisotropy and a greater degree of magnetically coupled carriers experiencing a reduction in mean free path from the applied magnetic field. Additionally, as previously observed in the linear absorption, increased inter-particle interactions between individual bornite PSNCs are expected to increase the degree of phonon−hole coupling and further enhance the observed $m^*$. The result is an increased value of 5.98 $m^*/m_e$ at fields >8 T. Large $g$-values have also been reported in dilute magnetic semiconductors due to the carriers coupling to magnetic spin.[75] By analogy to dilute magnetic semiconductors where the carrier is coupled to spins in the lattice, the field-dependent response of $m^*$ can be fitted to a Brillouin function in eq 10, assuming the relationship of the cyclotron resonance, $E_z$, and LSPR, such that

$$m^* = \frac{1}{2} N g_S \mu_B \left[ (2S+1)\coth\left( (2S+1)\frac{g_S \mu_B B}{2k_B T} \right) - \coth\left( \frac{g_S \mu_B B}{2k_B T} \right) \right] \quad (10)$$

where $N$ is a fitting parameter, $g_s$ is the Lande' $g$-factor, $\mu_B$ is the Bohr magneton, $S$ is the spin quantum number, $B$ is the magnetic field, $k_B$ is the Boltzmann constant, and $T$ is the temperature. A large $g$-value (14.3) is extracted from the experimental data fit in Figure 4, assuming $S = 1/2$ and $T = 40$ K. Similar magnetic dependence has been observed previously in dilute magnetic semiconductors[76] and recently in gold cluster interband transitions, where the thermally driven population of d-band carriers were reported to be involved.[77] The experimental data supports the coupling of the d-band spins and hole carriers in the 5:1 bornite through the spin-ordering structural transition.

## CONCLUSIONS

$Cu_5FeS_4$ PSNCs were examined by various optical, magnetic, and magneto-optical techniques in tandem to measure the effective mass of bornite directly and explain the origins of the observed field-dependent behavior. DFT and SQUID measurements highlighted that bornite exhibits an antiferromagnetic transition that leads to increased magnetocrystalline anisotropy and a coupling of the d-bands to the hole carriers in the conduction band via a p−d exchange mechanism. The exchange mechanism leads to a field-dependent $m^*$ value that, when fitted to a Brillouin function, yields a large $g$-value for the LSPR.

The $Cu_5FeS_4$ nanocrystal is confirmed to be a p-type semiconductor based on the VH-MCD data. The $m^*$ of the LSPR at 1.12 eV in $Cu_5FeS_4$ was quantified as 2.73 $m^*/m_e$ in the low-field regime and 5.98 $m^*/m_e$ in the high-field regime utilizing high-field VH-MCD. The observed field-dependent $m^*$ behavior was attributed to a substantial decrease in the carrier mean free path due to magnetocrystalline anisotropy, polaronic type coupling with native defects, and LSPR-enhanced magnetic anisotropy. Further work should be done to experimentally validate the anisotropy of $m^*$ proposed in


https://doi.org/10.1021/acs.jpcc.2c03459
J. Phys. Chem. C 2022, 126, 12669−12679

$Cu_5FeS_4$, as was previously done for anatase. The observation of an external magnetic field directly influencing the electronic transport properties in $Cu_5FeS_4$ PSNCs suggests the role of magnetocrystalline anisotropy on carrier transport in plasmonic and thermoelectric materials is under-investigated in nanomaterials.

## ■ ASSOCIATED CONTENT

### Supporting Information

The Supporting Information is available free of charge at https://pubs.acs.org/doi/10.1021/acs.jpcc.2c03459.

Drude modeling of $Cu_5FeS_4$ LSPR spectra, VT-MCD at 10 T, Zeeman energy fitting with $m^*$ acquisition description, linear $m^*$ approximation, TEM and p-XRD for 5 nm $Cu_5FeS_4$ PSNCs, MCD instrument calibration using Au nanoparticles, and full unmodified VH-MCD spectra are found in the ESI (PDF)

## ■ AUTHOR INFORMATION


### Corresponding Author

**Geoffrey F. Strouse** − *Department of Chemistry and Biochemistry, Florida State University, Tallahassee, Florida 32306, United States;* orcid.org/0000-0003-0841-282X; Email: gstrouse@fsu.edu

### Authors

**Jason E. Kuszynski** − *Department of Chemistry and Biochemistry, Florida State University, Tallahassee, Florida 32306, United States*

**Joshua C. Kays** − *Department of Biomedical Engineering, Boston University, Boston, Massachusetts 02215, United States*

**Carl R. Conti, III** − *Department of Chemistry and Biochemistry, Florida State University, Tallahassee, Florida 32306, United States*

**Stephen A. McGill** − *National High Magnetic Field Laboratory, Tallahassee, Florida 32310, United States*

**Allison M. Dennis** − *Department of Biomedical Engineering, Boston University, Boston, Massachusetts 02215, United States; Division of Materials Science & Engineering, Boston University, Boston, Massachusetts 02215, United States;* orcid.org/0000-0001-5759-9905

Complete contact information is available at: https://pubs.acs.org/10.1021/acs.jpcc.2c03459


### Author Contributions

CRediT: The manuscript was written through contributions of all authors. All authors have given approval to the final version of the manuscript. J.E.K.: Conceptualization, formal analysis, investigation, methodology, software, validation, visualization, writing—original draft, writing—review and editing. J.C.K.: Conceptualization, resources, writing—review and editing. C.R.C.: Conceptualization, funding acquisition, writing—review and editing. S.A.M.: Conceptualization, methodology, resources, supervision, writing—review and editing. A.M.D.: Resources, funding acquisition, supervision, writing—review and editing. G.F.S.: Conceptualization, funding acquisition, methodology, supervision, writing—original draft, writing—review and editing.

### Notes

The authors declare no competing financial interest.

## ■ ACKNOWLEDGMENTS

G.F.S., J.E.K., and C.R.C. wish to thank the National Science Foundation (DMR-1905757) "Tuning Plasmonic and Magneto-Plasmonic Behavior in 4-d Transition Metal Doped Indium Oxide". A.M.D. and J.C.K. wish to thank the National Institute of General Medical Sciences of the National Institutes of Health under Award Number R21GM135849 for funding. A portion of this work was performed at the National High Magnetic Field Laboratory, which is supported by the National Science Foundation Cooperative Agreement (DMR-1644779) and the state of Florida. The authors would also like to thank Neda Arabzadeh and Dr. Hedi Mattoussi for providing the gold nanoparticle standard and Dr. Tony Saucedo and Dr. Michael Shatruk for the SQUID data.

## ■ REFERENCES


(1) Kelly, K. L.; Coronado, E.; Zhao, L. L.; Schatz, G. C. The Optical Properties of Metal Nanoparticles: The Influence of Size, Shape, and Dielectric Environment. *J. Phys. Chem. B* **2003**, *107*, 668−677.

(2) Rycenga, M.; Cobley, C. M.; Zeng, J.; Li, W.; Moran, C. H.; Zhang, Q.; Qin, D.; Xia, Y. Controlling the Synthesis and Assembly of Silver Nanostructures for Plasmonic Applications. *Chem. Rev.* **2011**, *111*, 3669−3712.

(3) Amendola, V.; Pilot, R.; Frasconi, M.; Maragò, O. M.; Iatì, M. A. Surface Plasmon Resonance in Gold Nanoparticles: A Review. *J. Phys.: Condens. Matter* **2017**, *29*, No. 203002.

(4) Khanna, P. K.; Gaikwad, S.; Adhyapak, P. V.; Singh, N.; Marimuthu, R. Synthesis and Characterization of Copper Nanoparticles. *Mater. Lett.* **2007**, *61*, 4711−4714.

(5) Gutiérrez, Y.; Brown, A. S.; Moreno, F.; Losurdo, M. Plasmonics beyond Noble Metals: Exploiting Phase and Compositional Changes for Manipulating Plasmonic Performance. *J. Appl. Phys.* **2020**, *128*, No. 080901.

(6) Agrawal, A.; Cho, S. H.; Zandi, O.; Ghosh, S.; Johns, R. W.; Milliron, D. J. Localized Surface Plasmon Resonance in Semiconductor Nanocrystals. *Chem. Rev.* **2018**, *118*, 3121−3207.

(7) Fleischmann, M.; Hendra, P. J.; McQuillan, A. J. Raman Spectra of Pyridine Adsorbed at a Silver Electrode. *Chem. Phys. Lett.* **1974**, *26*, 163−166.

(8) Lodewijks, K.; Van Roy, W.; Borghs, G.; Lagae, L.; Van Dorpe, P. Boosting the Figure-Of-Merit of LSPR-Based Refractive Index Sensing by Phase-Sensitive Measurements. *Nano Lett.* **2012**, *12*, 1655−1659.

(9) Lemos de Souza, M.; Santos, D. P. dos.; Corio, P. Localized Surface Plasmon Resonance Enhanced Photocatalysis: An Experimental and Theoretical Mechanistic Investigation. *RSC Adv.* **2018**, *8*, 28753−28762.

(10) Mendelsberg, R. J.; Garcia, G.; Milliron, D. J. Extracting Reliable Electronic Properties from Transmission Spectra of Indium Tin Oxide Thin Films and Nanocrystal Films by Careful Application of the Drude Theory. *J. Appl. Phys.* **2012**, *111*, No. 063515.

(11) Faucheaux, J. A.; Stanton, A. L. D.; Jain, P. K. Plasmon Resonances of Semiconductor Nanocrystals: Physical Principles and New Opportunities. *J. Phys. Chem. Lett.* **2014**, *5*, 976−985.

(12) Jung, J.; Pedersen, T. G. Analysis of Plasmonic Properties of Heavily Doped Semiconductors Using Full Band Structure Calculations. *J. Appl. Phys.* **2013**, *113*, No. 114904.

(13) Schimpf, A. M.; Gunthardt, C. E.; Rinehart, J. D.; Mayer, J. M.; Gamelin, D. R. Controlling Carrier Densities in Photochemically Reduced Colloidal ZnO Nanocrystals: Size Dependence and Role of the Hole Quencher. *J. Am. Chem. Soc.* **2013**, *135*, 16569−16577.

(14) Valdez, C. N.; Braten, M.; Soria, A.; Gamelin, D. R.; Mayer, J. M. Effect of Protons on the Redox Chemistry of Colloidal Zinc Oxide Nanocrystals. *J. Am. Chem. Soc.* **2013**, *135*, 8492−8495.

(15) Conti, C. R.; McBride, J. R.; Strouse, G. F. Examining the Effect of Dopant Ionic Radius on Plasmonic M:ZnO Nanocrystals (M = $Al^{3+}$, $Ga^{3+}$, $In^{3+}$). *J. Phys. Chem. C* **2021**, *125*, 7772−7779.
(16) Conti, C. R., III.; Quiroz-Delfi, G.; Schwarck, J. S.; Chen, B.; Strouse, G. F. Carrier Density, Effective Mass, and Nuclear Relaxation Pathways in Plasmonic Sn:$In_2O_3$ Nanocrystals. *J. Phys. Chem. C* **2020**, *124*, 28220−28229.
(17) Liu, Z.; Beaulac, R. Nature of the Infrared Transition of Colloidal Indium Nitride Nanocrystals: Nonparabolicity Effects on the Plasmonic Behavior of Doped Semiconductor Nanomaterials. *Chem. Mater.* **2017**, *29*, 7507−7514.
(18) Carroll, G. M.; Schimpf, A. M.; Tsui, E. Y.; Gamelin, D. R. Redox Potentials of Colloidal N-Type ZnO Nanocrystals: Effects of Confinement, Electron Density, and Fermi-Level Pinning by Aldehyde Hydrogenation. *J. Am. Chem. Soc.* **2015**, *137*, 11163−11169.
(19) Lakhwani, G.; Roijmans, R. F. H.; Kronemeijer, A. J.; Gilot, J.; Janssen, R. A. J.; Meskers, S. C. J. Probing Charge Carrier Density in a Layer of Photodoped ZnO Nanoparticles by Spectroscopic Ellipsometry. *J. Phys. Chem. C* **2010**, *114*, 14804−14810.
(20) Rinehart, J. D.; Schimpf, A. M.; Weaver, A. L.; Cohn, A. W.; Gamelin, D. R. Photochemical Electronic Doping of Colloidal CdSe Nanocrystals. *J. Am. Chem. Soc.* **2013**, *135*, 18782−18785.
(21) Cohn, A. W.; Janßen, N.; Mayer, J. M.; Gamelin, D. R. Photocharging ZnO Nanocrystals: Picosecond Hole Capture, Electron Accumulation, and Auger Recombination. *J. Phys. Chem. C* **2012**, *116*, 20633−20642.
(22) Kays, J. C.; Conti, C. R.; Margaronis, A.; Kuszynski, J. E.; Strouse, G. F.; Dennis, A. M. Controlled Synthesis and Exploration of CuxFeS4 Bornite Nanocrystals. *Chem. Mater.* **2021**, *33*, 7408−7416.
(23) Kovalenko, M. V.; Manna, L.; Cabot, A.; Hens, Z.; Talapin, D. V.; Kagan, C. R.; Klimov, V. I.; Rogach, A. L.; Reiss, P.; Milliron, D. J.; et al. Prospects of Nanoscience with Nanocrystals. *ACS Nano* **2015**, *9*, 1012−1057.
(24) Liu, W.-D.; Yang, L.; Chen, Z.-G.; Zou, J. Promising and Eco-Friendly $Cu_2X$-Based Thermoelectric Materials: Progress and Applications. *Adv. Mater.* **2020**, *32*, No. 1905703.
(25) Shi, X.-L.; Zou, J.; Chen, Z.-G. Advanced Thermoelectric Design: From Materials and Structures to Devices. *Chem. Rev.* **2020**, *120*, 7399−7515.
(26) Guo, L.; Panderi, I.; Yan, D. D.; Szulak, K.; Li, Y.; Chen, Y.-T.; Ma, H.; Niesen, D. B.; Seeram, N.; Ahmed, A.; et al. A Comparative Study of Hollow Copper Sulfide Nanoparticles and Hollow Gold Nanospheres on Degradability and Toxicity. *ACS Nano* **2013**, *7*, 8780−8793.
(27) Wang, D.; Zhang, Y.; Guo, Q. Sub-10 Nm $Cu_5FeS_4$ Cube for Magnetic Resonance Imaging-Guided Photothermal Therapy of Cancer. *Int. J. Nanomedicine* **2018**, *13*, 7987−7996.
(28) Yuan, L.; Hu, W.; Zhang, H.; Chen, L.; Wang, J.; Wang, Q. $Cu_5FeS_4$ Nanoparticles With Tunable Plasmon Resonances for Efficient Photothermal Therapy of Cancers. *Front. Bioeng. Biotechnol.* **2020**, *8*, No. 21.
(29) Martinelli, A.; Lepore, G. O.; Bernardini, F.; Giaccherini, A.; Di Benedetto, F. The Puzzling Structure of $Cu_5FeS_4$ (Bornite) at Low Temperature. *Acta Crystallogr., Sect. B: Struct. Crystallogr. Cryst. Chem.* **2018**, *74*, 405−415.
(30) Kehoe, A. B.; Scanlon, D. O.; Watson, G. W. The Electronic Structure of Sulvanite Structured Semiconductors $Cu_3MCh_4$ (M = V, Nb, Ta; Ch = S, Se, Te): Prospects for Optoelectronic Applications. *J. Mater. Chem. C* **2015**, *3*, 12236−12244.
(31) Kehoe, A. B.; Scanlon, D. O.; Watson, G. W. Modelling Potential Photovoltaic Absorbers $Cu_3MCh_4$ (*M* = V, Nb, Ta; *Ch* = S, Se, Te) Using Density Functional Theory. *J. Phys.: Condens. Matter* **2016**, *28*, No. 175801.
(32) Ghosh, S.; Avellini, T.; Petrelli, A.; Kriegel, I.; Gaspari, R.; Almeida, G.; Bertoni, G.; Cavalli, A.; Scotognella, F.; Pellegrino, T.; Manna, L. Colloidal $CuFeS_2$ Nanocrystals: Intermediate Fe d-Band Leads to High Photothermal Conversion Efficiency. *Chem. Mater.* **2016**, *28*, 4848−4858.
(33) Gaspari, R.; Della Valle, G.; Ghosh, S.; Kriegel, I.; Scotognella, F.; Cavalli, A.; Manna, L. Quasi-Static Resonances in the Visible Spectrum from All-Dielectric Intermediate Band Semiconductor Nanocrystals. *Nano Lett.* **2017**, *17*, 7691−7695.
(34) Mantella, V.; Ninova, S.; Saris, S.; Loiudice, A.; Aschauer, U.; Buonsanti, R. Synthesis and Size-Dependent Optical Properties of Intermediate Band Gap $Cu_3VS_4$ Nanocrystals. *Chem. Mater.* **2019**, *31*, 532−540.
(35) Hartstein, K. H.; Schimpf, A. M.; Salvador, M.; Gamelin, D. R. Cyclotron Splittings in the Plasmon Resonances of Electronically Doped Semiconductor Nanocrystals Probed by Magnetic Circular Dichroism Spectroscopy. *J. Phys. Chem. Lett.* **2017**, *8*, 1831−1836.
(36) Hsu, S.-W.; Ngo, C.; Tao, A. R. Tunable and Directional Plasmonic Coupling within Semiconductor Nanodisk Assemblies. *Nano Lett.* **2014**, *14*, 2372−2380.
(37) Qiu, P.; Zhang, T.; Qiu, Y.; Shi, X.; Chen, L. Sulfide Bornite Thermoelectric Material: A Natural Mineral with Ultralow Thermal Conductivity. *Energy Environ. Sci.* **2014**, *7*, 4000−4006.
(38) Giannozzi, P.; Baroni, S.; Bonini, N.; Calandra, M.; Car, R.; Cavazzoni, C.; Ceresoli, D.; Chiarotti, G. L.; Cococcioni, M.; Dabo, I.; et al. QUANTUM ESPRESSO: A Modular and Open-Source Software Project for Quantum Simulations of Materials. *J. Phys.: Condens. Matter* **2009**, *21*, No. 395502.
(39) Monkhorst, H. J.; Pack, J. D. Special Points for Brillouin-Zone Integrations. *Phys. Rev. B* **1976**, *13*, 5188−5192.
(40) Li, D.; Barreteau, C.; Castell, M. R.; Silly, F.; Smogunov, A. Out- versus in-Plane Magnetic Anisotropy of Free Fe and Co Nanocrystals: Tight-Binding and First-Principles Studies. *Phys. Rev. B* **2014**, *90*, No. 205409.
(41) Martinelli, A.; Lepore, G. O.; Bernardini, F.; Giaccherini, A.; Di Benedetto, F. The Puzzling Structure of $Cu_5FeS_4$ (Bornite) at Low Temperature. *Acta Crystallogr., Sect. B: Struct. Sci., Cryst. Eng. Mater.* **2018**, *74*, 405−415.
(42) Borgheresi, M.; Di Benedetto, F.; Caneschi, A.; Pratesi, G.; Romanelli, M.; Sorace, L. *An EPR and SQUID Magnetometry Study of Bornite* **2007**, *34*, 609−619.
(43) Giamarchi, T.; Rüegg, C.; Tchernyshyov, O. Bose−Einstein Condensation in Magnetic Insulators. *Nature Phys* **2008**, *4*, 198−204.
(44) Dahlman, C. J.; Agrawal, A.; Staller, C. M.; Adair, J.; Milliron, D. J. Anisotropic Origins of Localized Surface Plasmon Resonance in N-Type Anatase $TiO_2$ Nanocrystals. *Chem. Mater.* **2019**, *31*, 502−511.
(45) Lee, S.; Ghosh, S.; Hoyer, C. E.; Liu, H.; Li, X.; Holmberg, V. C. Iron-Content-Dependent, Quasi-Static Dielectric Resonances and Oxidative Transitions in Bornite and Chalcopyrite Copper Iron Sulfide Nanocrystals. *Chem. Mater.* **2021**, *33*, 1821−1831.
(46) Prandini, G.; Marrazzo, A.; Castelli, I. E.; Mounet, N.; Marzari, N. Precision and Efficiency in Solid-State Pseudopotential Calculations. *npj Comput. Mater.* **2018**, *4*, No. 72.
(47) Garrity, K. F.; Bennett, J. W.; Rabe, K. M.; Vanderbilt, D. Pseudopotentials for High-Throughput DFT Calculations. *Comput. Mater. Sci.* **2014**, *81*, 446−452.
(48) Kucukbenli, E.; Monni, M.; Adetunji, B. I.; Ge, X.; Adebayo, G. A.; Marzari, N.; de Gironcoli, S.; Corso, A. D. Projector Augmented-Wave and All-Electron Calculations across the Periodic Table: A Comparison of Structural and Energetic Properties. 2014, arXiv:1404.3015. arXiv.org e-Print archive. https://arxiv.org/abs/1404.3015.
(49) Ando, K.; Munekata, H. Magneto-Optical Study of Spin-Carrier Interactions in (In,Mn)As. *J. Magn. Magn. Mater.* **2004**, *272*−*276*, 2004−2005.
(50) Oak, Hang Nam.; Baek, Kyung Seon.; Jo, Youri. Superparamagnetic Relaxation in $Cu_5FeS_4$. *Solid State Commun.* **1996**, *100*, 467−470.
(51) Jagadeesh, M. S.; Nagarathna, H. M.; Montano, P. A.; Mohindar, S. Seehra. Magnetic and Mössbauer Studies of Phase Transitions and Mixed Valences in Bornite ($Cu_{4.5}Fe_{1.2}S_{4.7}$). *Phys. Rev. B: Condens. Matter Mater. Phys.* **1981**, *23*, 2350−2356.


https://doi.org/10.1021/acs.jpcc.2c03459
J. Phys. Chem. C 2022, 126, 12669−12679

(52) Townsend, M. G.; Gosselin, J. R.; Tremblay, R. J.; Tremblay, R. J.; Ripley, L. G.; Carson, D. W.; Muir, W. B. A Magnetic and Mössbauer Study of Magnetic Ordering and Vacancy Clustering in $Cu_5FeS_4$. *J. Phys. Chem. Solids* **1977**, *38*, 1153−1159.
(53) Oak, H. N.; Baek, K. S.; Jo, Y. Superparamagnetic Relaxation in $Cu_5FeS_4$. *Solid State Commun.* **1996**, *100*, 467−470.
(54) Paunović, N.; Popović, Z. V.; Dohčević-Mitrović, Z. D. Superparamagnetism in Iron-Doped $CeO_{2-y}$ Nanocrystals. *J. Phys.: Condens. Matter* **2012**, *24*, No. 456001.
(55) Sil, S.; Datta, J.; Das, M.; Jana, R.; Halder, S.; Biswas, A.; Sanyal, D.; Ray, P. P. Bias Dependent Conduction and Relaxation Mechanism Study of $Cu_5FeS_4$ Film and Its Significance in Signal Transport Network. *J Mater Sci: Mater Electron* **2018**, *29*, 5014−5024.
(56) Stephens, P. J. Theory of Magnetic Circular Dichroism. *J. Chem. Phys.* **1970**, *52*, 3489−3516.
(57) Mason, W. R. *A Practical Guide to Magnetic Circular Dichroism Spectroscopy: Mason/MCD Spectroscopy*; John Wiley & Sons, Inc.: Hoboken, NJ, USA, 2007.
(58) Han, B.; Gao, X.; Lv, J.; Tang, Z. Magnetic Circular Dichroism in Nanomaterials: New Opportunity in Understanding and Modulation of Excitonic and Plasmonic Resonances. *Adv. Mater.* **2020**, *32*, No. 1801491.
(59) Radovanovic, P. R.; Gamelin, D. R. Magnetic Circular Dichroism Spectroscopy of $Co^{2+}$:CdS Diluted Magnetic Semiconductor Quantum Dots. In *Nanoscale Optics and Applications*; SPIE, 2002; Vol. *4809*, pp 51−61.
(60) Ando, K.; Saito, H.; Agarwal, K. C.; Debnath, M. C.; Zayets, V. Origin of the Anomalous Magnetic Circular Dichroism Spectral Shape in Ferromagnetic $Ga_{1-x}Mn_xAs$: Impurity Bands inside the Band Gap. *Phys. Rev. Lett.* **2008**, *100*, No. 067204.
(61) Ando, K.; Takahashi, K.; Okuda, T.; Umehara, M. Magnetic Circular Dichroism of Zinc-Blende-Phase MnTe. *Phys. Rev. B* **1992**, *46*, 12289−12297.
(62) Shiratsu, T.; Yao, H. Magnetic Circular Dichroism (MCD) in Silver Nanocubes with Different Sizes. *Chem. Phys. Lett.* **2018**, *706*, 607−612.
(63) Sheikholeslami, S.; Jun, Y.; Jain, P. K.; Alivisatos, A. P. Coupling of Optical Resonances in a Compositionally Asymmetric Plasmonic Nanoparticle Dimer. *Nano Lett.* **2010**, *10*, 2655−2660.
(64) Luo, Y.; Dube, L.; Zhou, Y.; Zou, S.; Zhao, J. Plasmonic Coupling in Single Flower-like Gold Nanoparticle Assemblies. *Prog. Nat. Sci.: Mater. Int.* **2016**, *26*, 449−454.
(65) Runnerstrom, E. L.; Bergerud, A.; Agrawal, A.; Johns, R. W.; Dahlman, C. J.; Singh, A.; Selbach, S. M.; Milliron, D. J. Defect Engineering in Plasmonic Metal Oxide Nanocrystals. *Nano Lett.* **2016**, *16*, 3390−3398.
(66) Safin, F.; Maslov, V.; Gromova, Y.; Korsakov, I.; Kolesova, E.; Dubavik, A.; Cherevkov, S.; Gun'ko, Y. K. Investigation of Magnetic Circular Dichroism Spectra of Semiconductor Quantum Rods and Quantum Dot-in-Rods. *Nanomaterials* **2020**, *10*, 1059.
(67) Neese, F.; Solomon, E. I. MCD *C* -Term Signs, Saturation Behavior, and Determination of Band Polarizations in Randomly Oriented Systems with Spin $S \geq 1/2$. Applications to $S = 1/2$ and $S = 5/2$. *Inorg. Chem.* **1999**, *38*, 1847−1865.
(68) Kasap, S. O. *Principles of Electronic Materials and Devices*, 4th ed.; McGraw-Hill, a business unit of The McGraw-Hill Companies, Inc: New York, NY, 2018.
(69) Goh, S. W.; Buckley, A. N.; Lamb, R. N.; Rosenberg, R. A.; Moran, D. The Oxidation States of Copper and Iron in Mineral Sulfides, and the Oxides Formed on Initial Exposure of Chalcopyrite and Bornite to Air. *Geochim. Cosmochim. Acta* **2006**, *70*, 2210−2228.
(70) Schneider, S. S. B. Piepho and P. Schatz: Group Theory in Spectroscopy With Applications to Magnetic Circular Dichroism, Aus Der Reihe: Wiley Interscience Monographs in Chemical Physics, John Wiley + Sons, New York, Chichester, Brisbane, Toronto, Singapore 1983. 634 Seiten, Preis: £ 65.75. *Berichte der Bunsengesellschaft für physikalische Chemie* **1984**, *88*, 1023.
(71) Shen, Y.; Li, C.; Huang, R.; Tian, R.; Ye, Y.; Pan, L.; Koumoto, K.; Zhang, R.; Wan, C.; Wang, Y. Eco-Friendly p -Type $Cu_2SnS_3$ Thermoelectric Material: Crystal Structure and Transport Properties. *Sci. Rep.* **2016**, *6*, No. 32501.
(72) Pavan Kumar, V.; Barbier, T.; Lemoine, P.; Raveau, B.; Nassif, V.; Guilmeau, E. The Crucial Role of Selenium for Sulphur Substitution in the Structural Transitions and Thermoelectric Properties of $Cu_5FeS_4$ Bornite. *Dalton Trans.* **2017**, *46*, 2174−2183.
(73) Pineider, F.; Campo, G.; Bonanni, V.; Fernández, C. D. J.; Mattei, G.; Caneschi, A.; Gatteschi, D.; Sangregorio, C. Circular Magnetoplasmonic Modes in Gold Nanoparticles. *Nano Lett.* **2013**, *13*, 4785−4789.
(74) Kikuchi, Y.; Tanaka, T. Strengthen of Magnetic Anisotropy of Au/Co/Au Nanostructure by Surface Plasmon Resonance. *Sci. Rep.* **2019**, *9*, No. 8630.
(75) Magana, D.; Perera, S. C.; Harter, A. G.; Dalal, N. S.; Strouse, G. F. Switching-on Superparamagnetism in Mn/CdSe Quantum Dots. *J. Am. Chem. Soc.* **2006**, *128*, 2931−2939.
(76) Kamra, A.; Ghosh, B.; Ghosh, T. K. Spin Relaxation Due to Electron−Electron Magnetic Interaction in High Lande g-Factor Semiconductors. *J. Appl. Phys.* **2010**, *108*, No. 054505.
(77) Herbert, P. J.; Window, P.; Ackerson, C. J.; Knappenberger, K. L. Low-Temperature Magnetism in Nanoscale Gold Revealed through Variable-Temperature Magnetic Circular Dichroism Spectroscopy. *J. Phys. Chem. Lett.* **2019**, *10*, 189−193.




https://doi.org/10.1021/acs.jpcc.2c03459
J. Phys. Chem. C 2022, 126, 12669−12679